

## Doppler Imaging of stellar magnetic fields

### III. Abundance distribution and magnetic field geometry of $\alpha^2$ CVn<sup>\*</sup>

O. Kochukhov<sup>1</sup>, N. Piskunov<sup>1</sup>, I. Ilyin<sup>2</sup>, S. Ilyina<sup>2</sup>, and I. Tuominen<sup>2</sup>

<sup>1</sup> Uppsala Astronomical Observatory, Box 515, 751 20 Uppsala, Sweden

<sup>2</sup> Astronomy Division, Box 3000, 90014 University of Oulu, Finland

Received 13 November 2001 / Accepted 27 February 2002

**Abstract.** We used the new magnetic Doppler Imaging code to reconstruct the magnetic field geometry and surface abundance distributions for the classical magnetic CP star  $\alpha^2$  CVn. High-resolution spectropolarimetric observations in the Stokes  $I$  and  $V$  parameters were collected with the SOFIN échelle spectrograph at the Nordic Optical Telescope. This superb observational material in combination with the advanced modelling technique allowed to achieve the first simultaneous self-consistent mapping of the vector magnetic field and the abundance distributions of six chemical elements. In recovering the stellar magnetic distribution no prior assumptions about the field geometry or strength were made. Instead, we restricted possible solutions of the inverse problem by means of the multipolar regularization method which searches for the field map close to a general non-axisymmetric multipolar configuration but allows departures from this geometry if that is required by the observational data. We found that the magnetic field of  $\alpha^2$  CVn is dominated by a dipolar component and has a minor quadrupole contribution. The surface distributions of the chemical species form symmetric patterns which closely follow the magnetic geometry. This discovery constitutes one of the first direct observational constraints on the horizontal diffusion processes acting in the upper envelope of a strongly magnetized stellar atmosphere. In addition to the extensive magnetic Doppler Imaging analysis, we derived new accurate estimates of the atmospheric parameters and basic physical properties of  $\alpha^2$  CVn using the energy distribution, hydrogen line profiles and the recent Hipparchos parallax.

**Key words.** stars: chemically peculiar – stars: magnetic fields – stars: individual:  $\alpha^2$  CVn

#### 1. Introduction

Magnetic chemically peculiar (CP) A and B stars are generally characterized by the abnormal strengths of spectral lines of some chemical elements and possess strong, globally organized magnetic fields. Furthermore, CP stars often show remarkable variations of line strengths, light and magnetic field with periods ranging from a few days to many years. These periodic variations are interpreted within the phenomenological Oblique Rotator Model suggested by Stibbs (1950). In the framework of this hypothesis periodic variations of the magnetic CP stars are attributed to the rotational modulation due to an inhomogeneous distribution of chemical abundance, magnetic field and, consequently, the whole structure of the stellar photosphere over the stellar surface. These surface

inhomogeneities are generally non-axisymmetric with respect to the stellar rotational axis and therefore, as the star rotates, we see variations with its rotational period.

It is believed that the abnormal chemical composition of CP stars is limited only to the outer stellar envelopes and is produced by chemical diffusion (Michaud 1970). This phenomenon occurs due to the imperfect balance between the forces of gravitational settling and radiative acceleration acting on each individual atom. If competing mixing processes, such as convection or a strong mass loss, fail to hamper diffusion drift, it enriches or depletes the line-forming region from the atoms of various trace elements. Chemical diffusion altered by a global magnetic field can produce surface abundance non-uniformities.

Although the Oblique Rotator Model and chemical diffusion together form a convincing basis for the qualitative interpretation of the magnetic CP phenomenon, many fundamental questions remain unanswered. For example, it is not at all clear what is the typical geometry of the global magnetic fields of the early-type stars. It was widely argued in the past that the magnetic fields of CP

---

Send offprint requests to: O. Kochukhov,  
e-mail: oleg@astro.uu.se

\* Based on observations obtained with the Nordic Optical Telescope (NOT) and Isaac Newton Telescope (INT), La Palma, Spain.

stars have predominantly a dipolar structure (Landstreet 1992), but the most recent studies (e.g. Bagnulo et al. 1999; Bagnulo & Landolfi 1999) hinted that more complicated non-axisymmetric field distributions may be more common. In addition, the detailed mechanism of the chemical diffusion in the presence of a magnetic field is unknown. Any attempt to build such a theory would face major difficulties in explaining scarce magnetic field measurements and surface chemical abundance maps, which, depending on a particular star and chemical element, may or may not correlate with each other.

Clearly, the first fundamental step in resolving the puzzle of the magnetic CP stars would be a detailed simultaneous investigation of the surface abundance structures and the magnetic field topologies. In the past such studies were predominantly based on the Fourier analysis of the variation of the disk-integrated quantities, such as equivalent widths, radial velocities and longitudinal magnetic field (e.g. Deutsch 1958; Pyper 1969). More recent investigations, such as the one presented by Kuschnig et al. (1999), attempt to reconstruct surface abundance distributions with the Doppler Imaging (DI) method. This technique uses a well-structured computational algorithm, which inverts time-series of high-resolution profiles of spectral lines into maps of chemical abundance spots. Doppler Imaging studies do not usually take into account the presence of the magnetic field and try to avoid strongly magnetic CP stars. On the other hand, the magnetic field topology is frequently inferred from the analysis of various magnetic observables under the assumption of a homogeneous surface abundance distribution. However, magnetic and chemical structures are closely related to each other and in most interesting CP stars (those that feature both strong magnetic fields and highly inhomogeneous abundance distribution) modelling of the global magnetic field must take into account non-uniform sampling over the stellar disk due to the presence of the abundance spots. Conversely, unaccounted magnetic splitting and intensification can severely bias abundance maps produced for the magnetic stars using conventional non-magnetic abundance mapping algorithms.

The most promising tool for an accurate modelling of the stellar magnetic fields and related surface structures is magnetic Doppler Imaging (MDI) based on a direct inversion of a time-series of high-resolution Stokes profiles. In Piskunov & Kochukhov (2002, hereafter Paper I) we described the new MDI code `INVERS10`, aimed at the simultaneous and self-consistent recovery of the stellar magnetic field vector map and the distribution of the chemical abundance over the stellar surface. Our code incorporates the latest developments in polarized radiative transfer algorithms, optimization and parallel computing methods. It is the first DI code that uses the accurate numerical solution of the polarized radiative transfer equation and allows to recover an arbitrary magnetic field distribution from the full Stokes vector datasets. Numerical experiments, presented in our second paper (Kochukhov & Piskunov 2002, hereafter Paper II), confirmed that, given high-quality

observations of line profiles in the four Stokes parameters, `INVERS10` is capable of reconstructing the abundance and magnetic field topology without the usual multipolar assumption about the geometry of the global stellar magnetic field. Additional tests demonstrated that a modified version of the MDI code can extract useful information about the magnetic and abundance surface structures even from the rotational modulation of the Stokes  $I$  and  $V$  alone. It is important to remember that today even the best four Stokes parameter observations of early-type magnetic stars (Wade et al. 2000a) do not have the resolution and the  $S/N$  ratio required for magnetic DI. On the other hand, high-quality datasets limited to the Stokes  $I$  and  $V$  parameters can more easily be collected with a number of modern high-resolution échelle spectrographs equipped with spectropolarimetric devices. Therefore, this modified version of our MDI code can readily be applied to the existing observations and used to infer properties of the surface structures in the magnetic CP stars. Here we present the first attempt to use `INVERS10` for the modelling of Stokes  $I$  and  $V$  profiles of the prototypical magnetic CP star  $\alpha^2$  CVn.

$\alpha^2$  CVn (= HD 112413 = HR 4915) was the first bright A star classified as chemically peculiar. Since the beginning of the 20th century much effort has been devoted to the description of the variations of its radial velocity, line strengths and longitudinal magnetic field. Previous detailed investigations of the magnetic field topology and chemical inhomogeneities (Pyper 1969; Khokhlova & Pavlova 1984) were based on a separate, inconsistent analysis of the magnetic and abundance observables. These studies provided only a coarse estimate of the magnetic geometry of  $\alpha^2$  CVn and yielded maps showing surface variations of equivalent width, but not absolute abundance distributions. Thus, we decided to choose  $\alpha^2$  CVn as the first target for the application of our MDI code.

Our paper is organized as follows. In Sect. 2 we describe acquisition and reduction of the high-resolution Stokes  $I$  and  $V$  spectra and other observational data. Next, in Sect. 3 we derive fundamental parameters of  $\alpha^2$  CVn. Modifications of the MDI code, determination of the projected stellar rotational velocity and a description of the DI results are given in Sect. 4. The paper ends with the Discussion (Sect. 5), where we compare our results with the outcome of the theoretical diffusion calculations and outline main advantages of the MDI technique over other modern methods of inferring the structure of the global stellar magnetic fields.

## 2. Observations and data reduction

### 2.1. High-resolution Stokes $I$ and $V$ spectra

Spectropolarimetric observations of  $\alpha^2$  CVn were obtained in 1996–1998 with the SOFIN instrument at the 2.56 m Nordic Optical Telescope (NOT). SOFIN is a high-resolution échelle spectrograph, mounted at the Cassegrain focus of NOT (Tuominen et al. 1999). It is

equipped with three cameras providing different resolving powers. Spectra of  $\alpha^2$  CVn were collected using the second camera, which allows to reach a resolution  $R = \lambda/\Delta\lambda \approx 80\,000$ . Most observations were obtained with a  $1152 \times 298$  pixel EEV CCD detector, allowing to register about 12 échelle orders, partially covering the range from 4000 to 7000 Å. The length of an individual order depends on the wavelength, but is typically about 40 Å.

Left and right circularly polarized spectra were acquired with the Stokesmeter, similar to the one described by Plachinda & Tarasova (1999). It consists of an achromatic (4000–6800 Å) rotateable quarter-wave plate, a beam splitter, made of a calcite plate, and a fixed achromatic quarter-wave plate on exit which converts the linearly polarized light into circularly polarized light to avoid linear polarized light attenuation on the échelle. The angle of the rotateable quarter-wave plate on the entrance is controlled by a stepping motor. The thickness of the calcite defines the image separation of  $3''$  on the slit. The two circularly polarized beams lead to two parallel spectra on the detector. Since the orders lie too close to each other on the CCD, the orders of the two stellar images would overlap. Thus, the two beams had to be observed in separate exposures. For accurate circular polarization measurements 4 exposures of  $\alpha^2$  CVn were usually obtained: each of the two beams was exposed twice with the quarter-wave plate rotated by  $90^\circ$  in between. This allowed to minimize instrumental effects caused by misalignments of the retarder axis relative to the calcite and the wavelength dependency of the retarder axis orientation. In the second image, taken with the quarter-wave plate rotated by  $90^\circ$ , these instrumental effects change sign, and can be cancelled by averaging the two images.

Since each beam is observed in a separate exposure, each image is a normal échelle spectrum, and no special reduction technique had to be developed. All reductions were done with the 4A software package (Ilyin 2000). The reduction included bias subtraction, pixels sensitivity correction with the help of a master flat field image, subtraction of the scattered light approximated by a 2D-smoothing spline, and weighted extraction of the orders with the subsequent elimination of cosmic spikes. The wavelength calibration was based upon two Th-Ar exposures acquired before and after each stellar exposure and made use of the whole set of comparison Th-Ar lines in all orders of the échelle frame.

The calibration also included corrections for small shifts between the comparison spectra and the stellar images using telluric lines in several orders. This drift of the spectrograph reference frame is caused by the difference in setting the star on the slit, temporal variations of the seeing and bending of the Cassegrain-mounted spectrograph during the telescope movement, all resulting in a spurious shift of spectral lines from one exposure to the other. This effect leads to additional “instrumental” polarization effect since each beam is exposed separately in time. Ilyin & Duemmler (1999) discussed how these shifts can be corrected very accurately using sharp telluric features.

**Table 1.** SOFIN observations of  $\alpha^2$  CVn.

Dates	Number of spectra	Range of $S/N$
26/10/1996–27/10/1996	4	170–220
22/11/1996–01/12/1996	32	160–300
22/06/1997–27/06/1997	24	200–230
15/08/1997–22/08/1997	32	190–260
12/12/1997–25/12/1997	24	190–310
15/03/1998–20/03/1998	16	170–250
02/07/1998–07/07/1998	24	160–190

An upper limit of the spurious Stokes  $V$  signal was estimated from the analysis of SOFIN circular polarization measurements of  $\alpha$  Boo. This non-magnetic star was observed during the same nights and using the same instrumental configuration as we used for  $\alpha^2$  CVn. It was found that the instrumental polarization never exceeded the statistical noise and was smaller than a few times  $10^{-3}$ .

We also obtained a few unpolarized spectra of sharp-lined non-magnetic Am and superficially normal A stars for the purpose of refining relative oscillator strengths of spectral lines used in the magnetic DI.

Table 1 gives a summary of our spectropolarimetric observations. It lists the dates of the observing runs, the number of spectra obtained and the typical range of signal-to-noise ratios of the individual left and right circularly polarized spectra. Observations of  $\alpha^2$  CVn were phased according to the ephemeris of Farnsworth (1932):

$$\text{JD} = 2419869.720 + 5^{\text{d}}46939 \cdot E, \quad (1)$$

which refers to the phase of the maximum intensity of Eu II spectral lines. 156 individual exposures of left and right circularly polarized beams were averaged to produce 41 pairs of Stokes  $I$  and  $V$  spectra. Observations with phase differences less than 0.02 were further coadded. Wavelength settings were not identical in the 7 observing runs listed in Table 1, and depending on the wavelength region we ended up using in the magnetic Doppler Imaging Stokes  $I$  and  $V$  profiles from 20 to 27 rotational phases.

To our knowledge, the SOFIN observations of  $\alpha^2$  CVn comprise the most extensive spectropolarimetric dataset ever obtained for a magnetic CP star and the first systematic Stokes  $I$  and  $V$  stellar observations at such high spectroscopic resolution. We note that the latter is indeed required for Doppler imaging analyses of magnetic stars with  $v_e \sin i \leq 20 \text{ km s}^{-1}$ .

## 2.2. Hydrogen Balmer lines and spectrophotometry

In addition to the high-resolution spectropolarimetry with SOFIN we obtained several unpolarized spectra of  $\alpha^2$  CVn with the MUSICOS échelle spectrograph at the 2.5 m Isaac Newton Telescope (INT).  $\alpha^2$  CVn was observed during 4 nights in May 1999 using a  $2048 \times 2048$  pixel CCD

**Table 2.** MUSICOS observations of  $\alpha^2$  CVn.

Date	Phase	$S/N$
27/05/1999	0.399	220
28/05/1999	0.593	230
29/05/1999	0.783	140
30/05/1999	0.957	120

detector, which allowed us to record 91 échelle orders covering the spectral region 3500–9200 Å without gaps at the resolution  $R \approx 30\,000$ . Acquisition dates, corresponding rotational phases of  $\alpha^2$  CVn and  $S/N$  ratios are listed in Table 2. MUSICOS spectra of  $\alpha^2$  CVn were reduced using standard échelle reduction procedures in the IRAF package. We extracted hydrogen line profiles of the first three Balmer lines from these observations and analysed a few other spectral lines located in the wavelength regions, not covered by the SOFIN spectra.

Accurate continuum normalization is crucial for the analysis of hydrogen lines in the spectra of A-type stars. Extraction of the Balmer lines from échelle observations is further complicated by the bell-like shape of the continuum in uncorrected échelle orders. Although we successfully used flat-field lamp exposures for removing pixel-to-pixel variations of the CCD sensitivity as well as for correcting fringing effects, we found that the shape of the blaze function in the flat-field spectra differed substantially from the observations of fast-rotating early-type stars. Therefore, the continuum in the stellar spectra could not be established using flat-field exposures. In order to overcome this problem we constructed artificial flat fields directly from the blaze function shape of the stellar exposures. Assuming that the relation between the blaze shapes of consecutive échelle orders is a smoothly changing function, we iteratively fitted 2D polynomials to the continuum regions of all orders excluding those containing hydrogen lines. The continuum in the latter échelle orders was subsequently determined by interpolation. Further details about the procedure of the continuum determination in the échelle spectra will be presented in our forthcoming paper (Barklem et al. 2002).

Careful comparison of the shapes of the Balmer lines in  $\alpha^2$  CVn spectra obtained at different rotational phases did not reveal any changes that would exceed the noise level of our observations. Therefore, we used the average of all four MUSICOS spectra in deriving atmospheric parameters of  $\alpha^2$  CVn (Sect. 3).

29 spectrophotometric scans of  $\alpha^2$  CVn were extracted from the catalogue of Adelman et al. (1989). These observations typically contain between 15 and 21 spectral points in the 3390–7850 Å wavelength region. All scans are normalized to the stellar magnitude at  $\lambda$  5000 Å. Since we were primarily interested in using the flux distribution for refining the atmospheric parameters of  $\alpha^2$  CVn, we averaged all the scans. This approach was justified by the absence of any systematic variations of the *normalized*

$\alpha^2$  CVn flux distributions with rotational phase. In fact, the scatter of individual spectrophotometric scans around the mean value does not exceed 0.01–0.02 mag, which is comparable with the observational uncertainty and accuracy of the theoretical fit.

### 3. Fundamental stellar parameters

As a starting point, we adopted the atmospheric parameters of  $\alpha^2$  CVn from the recent study of Ryabchikova et al. (1999), who found  $T_{\text{eff}} = 11\,500$  K and  $\log g = 4.0$ . Using these values of the effective temperature and surface gravity as the initial guess we then adjusted the stellar parameters by fitting the hydrogen Balmer lines and the energy distribution between 3390 and 7850 Å. All model atmospheres and theoretical flux distributions were calculated with the ATLAS9 code of Kurucz (1993) using an opacity distribution function with 10 times solar metal abundance. Piskunov & Kupka (2001) confirmed that abundance peculiarities typical for  $\alpha^2$  CVn are sufficiently small to justify the use of the models with scaled solar abundance table. In model atmosphere calculations we used a microturbulent velocity of  $4 \text{ km s}^{-1}$ . Although real microturbulent motions in the atmospheres of magnetic CP stars are probably inhibited by the strong magnetic field, we used the enhanced microturbulence in the model atmosphere calculations in order to mimic an increase in overall line opacity due to the magnetic intensification. On the other hand, zero microturbulence was used for the spectrum synthesis calculations throughout this paper. Hydrogen line profiles were computed with the BALMER code (Peterson 1969), modified to include the recent Stark broadening calculations by Stehlé (1994), instead of the Vidal et al. (1973) Stark broadening tables.

Around spectral class A0, the hydrogen lines reach their maximum strength and are mostly sensitive to the surface gravity. We found that the first three Balmer lines in  $\alpha^2$  CVn spectrum are well fitted with  $\log g = 3.9 \pm 0.1$  (see Figs. 1a-c), with  $H\alpha$  indicating slightly larger surface gravity than  $H\beta$  and  $H\gamma$ . The surface gravity obtained in our study is in good agreement with the other recent spectroscopic determination by Žižňovský & Zverko (1995), who found  $\log g = 3.8$  from the  $H\beta$  profile of  $\alpha^2$  CVn.

The flux distribution of  $\alpha^2$  CVn, in particular the size of the Balmer jump, is a useful indicator of the effective temperature. Using the average flux distribution extracted from the Adelman et al. (1989) catalogue we derived  $T_{\text{eff}} = 11\,600 \pm 150$  K. Figure 1d compares the observed and theoretical spectrophotometry. The overall shape of the energy distribution is fitted fairly well. The remaining discrepancies between observations and theoretical predictions in the region between the Balmer jump and  $H\gamma$  and redwards of  $H\alpha$  are probably due to the missing blue and ultraviolet line opacity and the difference between the real  $\alpha^2$  CVn abundance table and the scaled solar metal abundance assumption of the Kurucz’s ODFs.

The helium abundance is effectively another atmospheric parameter in a model atmosphere analysis of the

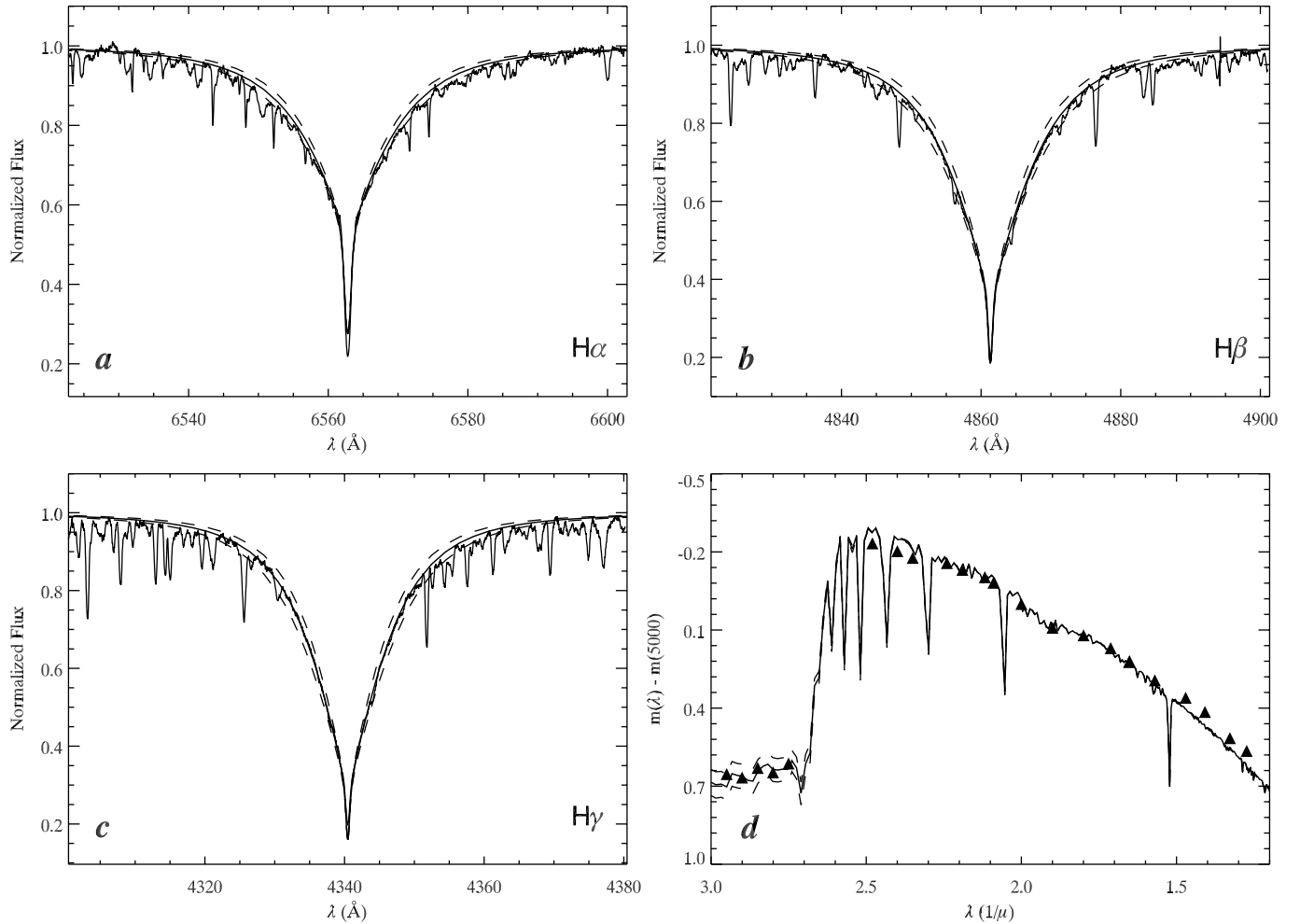


**Fig. 1.** The comparison between the observed and the computed hydrogen H $\alpha$ , H $\beta$  and H $\gamma$  spectral lines (panels a–c), respectively). The thick solid lines correspond to the profiles calculated with  $T_{\text{eff}} = 11\,600$  K and  $\log g = 3.9$ , while the dashed lines illustrate the effect of changing the surface gravity by  $\pm 0.2$  dex. The lower right panel d) compares observed (triangles) and computed (lines) spectrophotometry. The thick solid line shows the energy distribution predicted by the model with  $T_{\text{eff}} = 11\,600$  K and  $\log g = 3.9$ , the dashed lines illustrate the effect of changing the effective temperature by  $\pm 200$  K.

chemically peculiar stars. Auer et al. (1966) showed that as long as a model atmosphere’s hydrostatic stratification is concerned, a change in He concentration is equivalent to a change in surface gravity. In other words, the spectroscopic gravity derived under the assumption of a solar He content must be corrected if the star is found to possess an anomalous He abundance. This has recently been confirmed by Leone & Manfrè (1997) in the analysis of He-weak late B stars. These authors illustrated how incorrect abundance assumptions could lead to large errors in the surface gravity derived from Balmer lines. Having this problem in mind we examined the MUSICOS spectra of  $\alpha^2$  CVn in the regions containing the strongest He I lines at  $\lambda$  4026, 4471 and 5876  $\text{\AA}$ . The latter He I absorption feature turned out to be the most suitable for the abundance determination because of the lack of blending by lines of iron-peak and rare-earth elements. The comparison between non-magnetic synthetic spectra computed with the SYNTH code (Piskunov 1992) and the average MUSICOS spectrum of  $\alpha^2$  CVn (see Fig. 2) led to the discovery of an

extreme He-poor nature of this prototype magnetic star. We found that absorption features at the position of the He I line are much narrower than stellar spectral lines and are almost entirely due to telluric lines. Further comparison of our observations with the telluric atlas by Wallace et al. (2000) strengthened this conclusion. Helium is depleted in the  $\alpha^2$  CVn atmosphere by at least 3 orders of magnitude with respect to the normal stellar He content:  $\log(N_{\text{He}}/N_{\text{tot}}) \leq -4.05$ . We derived the He abundance from the average of 4  $\alpha^2$  CVn spectra acquired at distinct rotational phases. Thus an extreme He deficiency is likely to be characteristic for the whole  $\alpha^2$  CVn surface. After the correction for the peculiar He abundance (see Auer et al. 1966) our estimate of the  $\alpha^2$  CVn spectroscopic gravity becomes  $\log g = 4.02 \pm 0.10$ .

The effective temperature and surface gravity that we determined for  $\alpha^2$  CVn correspond to the atmospheric structure averaged over the stellar disk and rotational period. Abundance spots and magnetic field can substantially modify the local atmospheric structure. Modelling

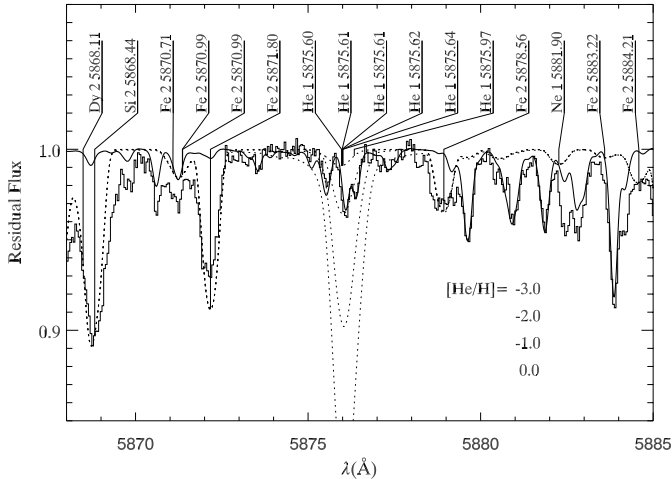


**Fig. 2.** The comparison between observations in the region of the He I 5876 Å line (histogram) and synthetic stellar spectra (dotted lines) of  $\alpha^2$  CVn generated for the range of He abundance from the solar value ( $[\text{He}/\text{H}] = 0.0$ ) down to 0.1% of the solar He content ( $[\text{He}/\text{H}] = -3.0$ ). The solid line shows a part of the telluric spectrum extracted from the atlas of Wallace et al. (2000). This spectrum has been broadened to match the resolution of the MUSICOS observations.

of this phenomenon is outside the scope of our study, but nevertheless we note that with the observational data available to us, we do not see a clear evidence for a rotational modulation of the Balmer lines or the shape of the flux distribution that could be parameterized with a phase dependent effective temperature and/or surface gravity. Thus, our atmospheric parameters are adequate through the whole rotational period of  $\alpha^2$  CVn. Furthermore, the absence of any strong rotational variability of the hydrogen lines or dramatic changes of the shape of the flux distribution suggests that local variations of the atmospheric structure have only a minor contribution to the rotational modulation of the metal lines. Therefore, we do not expect the abundance and magnetic field maps reconstructed for  $\alpha^2$  CVn in Sect. 4 to be severely affected by the local departures from the average atmospheric stratification that we adopted.

Gómez et al. (1998) determined the absolute visual magnitude of  $\alpha^2$  CVn,  $M_v = 0.3$ , using the Hipparchos parallax  $\pi = 29.60 \pm 1.04$  mas (ESA 1997). Applying a bolometric correction (Flower 1996) corresponding to the effective temperature of  $\alpha^2$  CVn we get the bolometric magnitude  $M_{\text{bol}} = -0.297 \pm 0.059$ . Effective temperature and bolometric magnitude are connected with the stellar luminosity and radius by the following relations:

$$\log(L/L_{\odot}) = -\frac{M_{\text{bol}} - M_{\text{bol}}^{\odot}}{2.5} \quad (2)$$

and

$$R/R_{\odot} = \left(\frac{L}{L_{\odot}}\right)^{1/2} \left(\frac{T_{\text{eff}}}{T_{\text{eff}}^{\odot}}\right)^{-2}, \quad (3)$$

where  $L_{\odot}$ ,  $M_{\text{bol}}^{\odot}$  and  $R_{\odot}$  are the solar luminosity, bolometric magnitude and radius. From Eqs. (2) and (3) we obtain

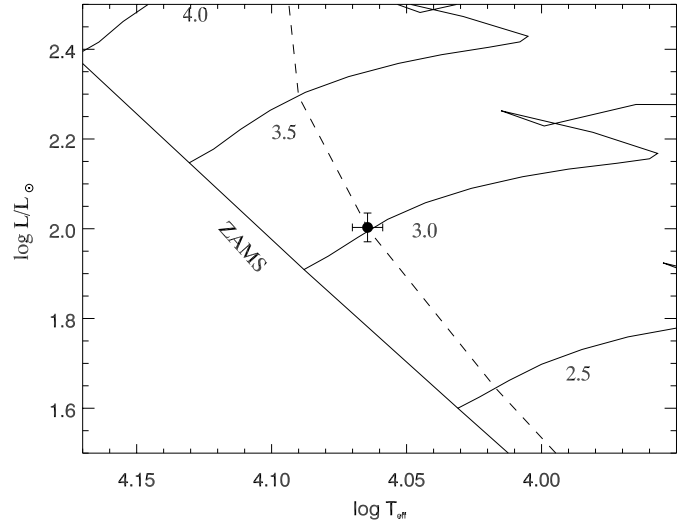


**Fig. 3.** The position of  $\alpha^2$  CVn in the H-R diagram is compared with the model evolutionary tracks of Schaller et al. (1992), computed for solar metallicity and masses  $M = 2.5, 3.0, 3.5$  and  $4.0 M_{\odot}$ . The dashed line shows the isochrone for  $\log(\text{Age}) = 8.145$ .

**Table 3.** Basic physical properties of  $\alpha^2$  CVn.

$T_{\text{eff}}$ (K)	$11600 \pm 150$
$\log g$	$4.02 \pm 0.10$
$L/L_{\odot}$	$100.7 \pm 5.5$
$R/R_{\odot}$	$2.488 \pm 0.094$
$M/M_{\odot}$	$3.010 \pm 0.065$
$\log(\text{Age})$	$8.145 \pm 0.075$

$\log(L/L_{\odot}) = 2.003 \pm 0.024$  and  $R/R_{\odot} = 2.488 \pm 0.094$ . The radius derived for  $\alpha^2$  CVn is formally consistent with  $R/R_{\odot} = 3.13 \pm 0.70$  obtained by Shallis et al. (1985) from the Infrared Flux Method. We note, however, that Shallis et al. used a too small effective temperature for  $\alpha^2$  CVn,  $T_{\text{eff}} = 10850$  K, thus their stellar radius was somewhat overestimated. Babu & Shylaja (1981) adopted a more realistic temperature in the Infrared Flux Method. Their estimate of the  $\alpha^2$  CVn radius, corrected for the improved parallax by Shallis et al. (1985), is  $R = 2.4 R_{\odot}$  and agrees better with our determination.

The stellar rotational period  $P$ , the radius  $R$ , the inclination of the rotational axis  $i$  and the projected rotational velocity  $v_e \sin i$  are related via the equation:

$$\sin i = \frac{P v_e \sin i R_{\odot}}{50.613 R}, \quad (4)$$

where the rotational period is measured in days and the rotational velocity in  $\text{km s}^{-1}$ . Adopting  $P = 5^{\text{d}}.46939$  and using the projected rotational velocity  $v_e \sin i = 17.4 \pm 0.5 \text{ km s}^{-1}$ , determined in Sect. 4.2, we find  $i = 49^{\circ}.1 \pm 3^{\circ}.1$  (or, equivalently,  $i = 130^{\circ}.9 \pm 3^{\circ}.1$ ). This value is in excellent agreement with an inclination angle  $i = 50^{\circ}$  that was derived in earlier detailed studies of the  $\alpha^2$  CVn surface structures (e.g. Pyper 1969; Khokhlova & Pavlova 1984).

The fundamental stellar parameters determined in this section allow us to uniquely locate the position of  $\alpha^2$  CVn in the theoretical H-R diagram. The comparison between our values of stellar luminosity and effective temperature and the predictions of the Schaller et al. (1992) evolutionary tracks is presented in Fig. 3 and yields a stellar mass  $M = 3.010 \pm 0.065 M_{\odot}$  and an age  $\log(\text{Age}) = 8.145 \pm 0.075$  yrs. Thus,  $\alpha^2$  CVn is a middle age star with about 40% of the main sequence lifetime behind.

From the relation between the surface gravity and the stellar mass,

$$\log g = \log g_{\odot} + \log(M/M_{\odot}) - 2 \log(R/R_{\odot}), \quad (5)$$

we get  $\log g = 4.13 \pm 0.04$ . This value is slightly larger than the spectroscopic surface gravity. If real, this discrepancy can indicate the modification of the hydrostatic equilibrium in the stellar atmosphere by an outward directed Lorentz force induced by the global magnetic field of  $\alpha^2$  CVn (Stepień 1978).

In Table 3 we summarize all fundamental stellar parameters of  $\alpha^2$  CVn derived in our study.

## 4. Magnetic and abundance mapping

### 4.1. Magnetic DI strategy

Our magnetic DI code `INVERS10` was originally developed for the MDI based on high-resolution observations in all four Stokes parameters. In this case the MDI problem has a unique solution and the role of regularization reduces to ensuring a numerical stability and a smooth convergence. However, when observations are limited to circular polarization only, the magnetic inversion becomes intrinsically non-unique and therefore a proper choice of regularization directly affects the solution. Careful analysis of the role of regularization in the magnetic DI (Paper I) and extensive numerical tests conducted in Paper II suggested that a modified version of our code can be also applied to the MDI of the magnetic CP stars based on Stokes  $I$  and  $V$  profiles alone. This is achieved by introducing a new type of regularization function, the *multipolar regularization*. Unlike conventional Tikhonov and Maximum Entropy regularization algorithms, which impose very general smoothness and informational criteria on an inverse problem solution, the multipolar regularization constrains the magnetic image by demanding its proximity to a best-fit multipolar field  $\mathbf{B}_{\text{model}}$ . The latter is evaluated during each iteration by expanding the current approximation of the stellar field into spherical harmonics up to the second order. The discrepancy measure between the current field and the best-fit multipolar field is scaled by the corresponding regularization parameter and added to the total discrepancy function, which also contains  $\chi^2$  of the fit to the observed Stokes profiles and other regularization functionals.

The second order multipolar expansion used in our code is equivalent to the approximation of the stellar magnetic field by a superposition of a dipole  $\mathbf{B}_d$  and

non-axisymmetric non-linear quadrupole  $\mathbf{B}_q$  (Landolfi et al. 1998). Due to this general quadrupole component the second order multipolar model defines a large family of global magnetic fields, many of those having rather complicated topology (e.g. Bagnulo & Landolfi 1999). However, in the magnetic DI of  $\alpha^2$  CVn we want to avoid solutions with unnecessary strong quadrupole components. We choose to find a magnetic field topology giving a good fit to the observed Stokes  $I$  and  $V$  profiles, but containing the least possible quadrupole contribution. In other words, we would like to retain some smoothness or simplicity constraints, similar to that the Tikhonov regularization imposes. A general form of the multipolar regularization introduced in Paper I encourages the magnetic distribution to be close to a multipolar topology, but not necessarily to the simplest one. An essential modification of the multipolar regularization procedure can be achieved by using unequal weights for dipole and higher multipolar components in constructing a model multipolar field:

$$\mathbf{B}_{\text{model}} = \mathbf{B}_d + \alpha_q \mathbf{B}_q + \dots, \quad (6)$$

where the coefficients  $\alpha$  scale higher multipoles by their increasing complexity or decreasing smoothness relative to that of a dipole. Smoothness of a multipolar component can be conveniently assessed by, for example, computing its Tikhonov regularization functional  $\mathcal{T}$ . Thus, we select the coefficients  $\alpha$  in such a way that they equalize the Tikhonov functionals of all multipolar components of a model field  $\mathbf{B}_{\text{model}}$ :

$$\alpha_i = \mathcal{T}(\mathbf{B}_d) / \mathcal{T}(\mathbf{B}_i). \quad (7)$$

We note, that this Tikhonov regularization is computed for a normalized magnetic distribution. Thus, it is the magnetic field topology, but not its absolute strength, that matters. For the particular case of the imaging of  $\alpha^2$  CVn we found  $\alpha_q \simeq 0.5$ . This parameter changes very little during the iterative inversion process.

Another important modification introduced in our MDI code concerns fitting measurements of the disk-average line-of-sight magnetic component – the mean longitudinal field. Until now, the longitudinal field was by far the most common observable used in determining the magnetic geometry of CP stars. It is measured either photopolarimetrically, from the wings of the hydrogen Balmer lines (Landstreet et al. 1975), or directly from the Stokes  $V$  profiles of individual metal lines (Mathys 1991). The latter method also allows to obtain other magnetic field observables, but it has the disadvantage of being affected by a non-uniform surface abundance distribution of chemical elements. As a result, the phase variation of the longitudinal field measured from metal lines is modulated by both the magnetic field and the non-uniform sampling of the stellar disk due to abundance spots. On the other hand, the longitudinal field inferred from the wings of Balmer lines is free from this problem, because one can safely assume hydrogen to be distributed homogeneously over the stellar surface. Therefore, it is rather straightforward

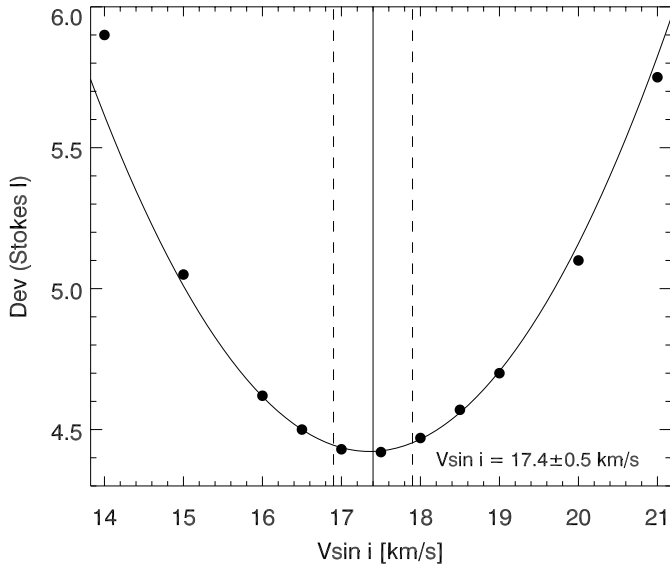


**Fig. 4.** The quality of the fit to Cr II Stokes  $I$  profiles is plotted against  $v_e \sin i$ . The solid curve shows the parabolic fit to the values between 16 and 19  $\text{km s}^{-1}$ . The vertical solid line corresponds to the optimal  $v_e \sin i = 17.4 \text{ km s}^{-1}$ , while the vertical dashed lines illustrate our estimate of the error in the derived projected rotational velocity.

to model photopolarimetric magnetic measurements and they can be used in combination with the high-resolution Stokes  $I$  and  $V$  data in the magnetic inversion. In practice, we fit photopolarimetric field measurements  $B_\ell^{\text{obs}}$  by evaluating the theoretical disk-average line-of-sight magnetic component  $B_\ell^{\text{calc}}$  and adding the total weighted deviation measure between the observed and computed longitudinal field,

$$\mathcal{R}_\ell = \Lambda_\ell \sum_i (B_\ell^{\text{calc}} - B_\ell^{\text{obs}})^2 / \sigma^2(B_\ell^{\text{obs}}), \quad (8)$$

to the total discrepancy function. Here  $\sigma(B_\ell^{\text{obs}})$  represents an accuracy of the individual photopolarimetric observations and  $\Lambda_\ell$  is a scalar, controlling the contribution of the functional  $\mathcal{R}_\ell$  to the total discrepancy function, which is minimized by INVERS10. As before (see Papers I and II), we select  $\Lambda_\ell$  is such a way, that at the convergence the contributions of all functionals would be approximately equal.

In all magnetic inversions presented in this paper we used the  $\alpha^2$  CVn magnetic measurements collected by Borra & Landstreet (1977) using a  $H\beta$  magnetometer. These authors obtained 21 longitudinal field observations with an accuracy ranging from 55 to 290 Gauss.

#### 4.2. Stellar rotational velocity

In Paper II we found that, similar to the conventional temperature and abundance DI, the magnetic inversion is sensitive to the adopted projected rotational velocity. Moderate errors in  $v_e \sin i$  can lead to the appearance of spurious abundance patterns and distort the magnetic

field topology. Nevertheless, we showed that these spurious solutions have significantly higher  $\chi^2$  of the fit to the observed Stokes profiles. This degradation of the fit quality is most clear for Stokes  $I$  spectra and can be used to select the optimal  $v_e \sin i$ . In order to determine  $v_e \sin i$  of  $\alpha^2$  CVn we reconstructed the magnetic field distribution and the chromium abundance map using 6 Cr II spectral lines and adopting different rotational velocities. Figure 4 shows the resulting plot of the total deviation for the Stokes  $I$  profiles versus  $v_e \sin i$ . From a parabolic fit to the points around the apparent minimum we determined  $v_e \sin i = 17.4 \pm 0.5 \text{ km s}^{-1}$ . This value is identical to the rotational velocity adopted in previous DI analyses of  $\alpha^2$  CVn (Khokhlova & Pavlova 1984; Glagolevskij et al. 1985) and agrees fairly well with the  $v_e \sin i$  found in several recent spectrum synthesis studies of this star (Ryabchikova et al. 1999; Takeda et al. 1999).

#### 4.3. Magnetic field geometry and surface distributions of Si, Cr, Fe

We reconstructed the silicon abundance distribution and the magnetic field geometry using two unblended Si II spectral lines at  $\lambda$  5957.56 and 5978.93 Å. A total of 20 rotational phases was available for mapping in this spectral region. Table 4 gives the atomic parameters of the Si II lines and other transitions that we used for the magnetic DI. All atomic parameters were extracted from the VALD database (Kupka et al. 1999) unless otherwise noted below. Landé factors of the lower and upper levels of the Si II lines were not listed in VALD, and we estimated these parameters using the LS-coupling approximation. The Zeeman splitting patterns and relative strengths of the magnetic components were computed for all spectral lines with the help of expressions given in Sobelman (1979) and using the Landé factors and  $J$  quantum numbers specified in Table 4.

The surface distribution of silicon and the magnetic field map recovered from the variations of the Si II lines are presented in Fig. 8. This figure and Fig. 11 show the abundance distribution and the magnetic field structure in the spherical projection. Figure 12 also gives an alternative cylindrical equidistant projection of all abundance maps obtained in our study. The comparison between observed and computed Stokes  $I$  and  $V$  profiles of the two Si II lines is shown in Fig. 5. At the top of each Stokes  $I$  and  $V$  panel of this figure, as well as Figs. 6, 7 and 10, we quote mean deviation  $\delta$  of the final fit to the observed spectra. INVERS10 typically achieved  $\delta \approx 0.4$ – $0.6\%$  in all Doppler inversions, while one would expect  $\delta \approx 0.3\%$  from the average quality of the spectra employed for DI. This remaining discrepancy can be attributed primarily to unrecognized blends and also to errors in atomic parameters and in continuum normalization.

The variations of the Stokes  $I$  and  $V$  parameters of the Si II lines are consistent with a dipole-like magnetic field geometry. We used the second order weighted multipolar

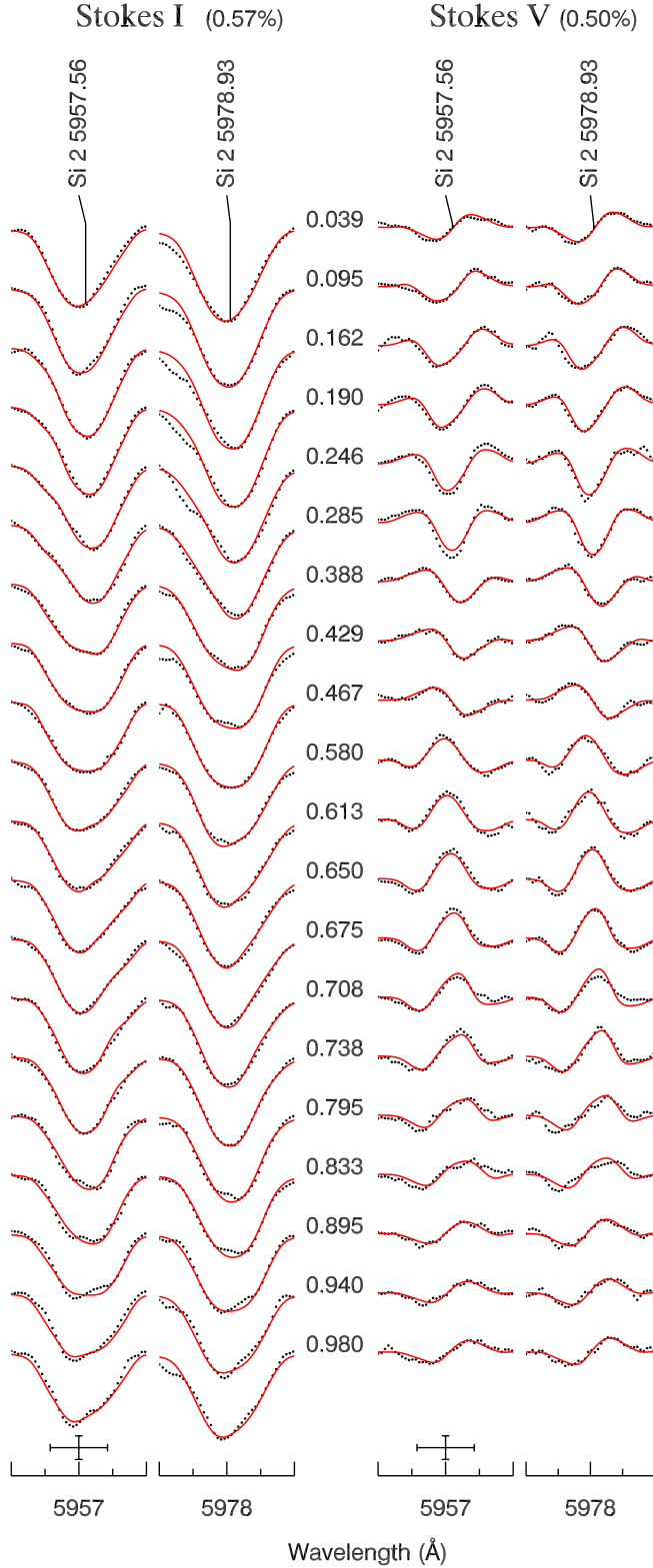


**Fig. 5.** The comparison between observed (dots) and computed (lines) Stokes *I* and *V* profiles of the Si II spectral lines. Spectra for the consecutive rotational phases are shifted in the vertical direction. Rotational phases are indicated in the column to the right of the Stokes *I* panel. The bars at the lower left corner of each panel correspond to 1 Å and 5% of the Stokes *I* continuum intensity. The number in brackets at the top of each panel quotes mean deviation relative to the continuum between observations and spectrum synthesis.

**Table 4.** Atomic parameters of the spectral lines used in magnetic DI of  $\alpha^2$  CVn.

$\lambda$ (Å)	$E_l$ (eV)	$\log(gf)$	$J_l$	$g_l$	$J_u$	$g_u$
Cl II						
4819.480	13.375	0.064	2.0	2.00	1.0	2.50
4819.756	15.679	-0.790	4.0	1.25	4.0	1.25
Si II						
5957.559	10.067	-0.301	0.5	0.67	0.5	2.00
5978.930	10.074	0.004	1.5	1.33	0.5	2.00
Ti II						
5381.015	1.566	-1.970	1.5	0.80	2.5	0.87
Cr II						
4812.337	3.864	-1.960	3.5	1.25	4.5	1.34
4824.127	3.871	-0.970	4.5	1.34	4.5	1.34
4836.229	3.858	-1.960	2.5	1.03	3.5	1.25
5274.964	4.071	-1.290	3.5	1.24	3.5	1.25
5279.876	4.073	-1.536	4.5	1.33	3.5	1.25
5280.054	4.074	-2.011	2.5	1.03	3.5	1.25
Fe II						
5026.806	10.308	-0.222	3.5	1.43	2.5	1.49
5035.708	10.288	0.606	4.5	1.45	5.5	1.38
5045.114	10.308	-0.134	3.5	1.43	2.5	1.29
5260.259	10.419	1.069	6.5	1.38	7.5	1.33
5387.063	10.522	0.518	5.5	1.27	6.5	1.29
5405.099	10.562	-1.010	4.5	1.18	4.5	1.24
5405.106	10.560	-0.268	0.5	0.00	1.5	1.37
5405.663	10.523	-0.435	2.5	1.29	2.5	1.18
5543.955	5.571	-3.095	2.5	0.86	1.5	1.14
5544.196	10.623	-0.230	2.5	0.58	3.5	1.20
5544.763	10.522	0.117	5.5	1.27	5.5	1.26
Nd III						
4927.420	0.461	-0.861	7.0	1.18	7.0	1.18
4942.580	0.632	-1.180	8.0	1.25	7.0	1.12
5677.120	0.632	-1.421	8.0	1.25	7.0	1.15

expansion (see Paper I) to characterise the global properties of the magnetic images produced by INVERS10. This analysis showed that the magnetic field, reconstructed using the Si II lines, was close to a superposition of a dipole with the polar strength  $B_d = 6.14$  kG and orientation  $\beta_d = 107^\circ.5$  and  $\gamma_d = 186^\circ.5$  (see Paper I for the detailed explanation of the multipolar parameterization that we use) and a weak quadrupole component ( $B_q = 1.18$  kG). The silicon abundance distribution is dominated by the two spots of Si overabundance ( $\log(N_{\text{Si}}/N_{\text{tot}}) \approx -3.0$ ) located at longitudes<sup>1</sup>  $l = 90^\circ$  and  $300^\circ$  and latitude

<sup>1</sup> Similar to Papers I and II we count stellar longitudes  $l$  from  $0^\circ$  to  $360^\circ$  in the direction of the stellar rotation. Phase zero corresponds to  $l = 0^\circ$ . Latitudes  $b$  change between  $-90^\circ$  at the invisible rotational pole up to  $+90^\circ$  at the visible pole.

$b \approx 30^\circ$ . These spots merge at high stellar latitudes forming a semi-ring of Si overabundance around the negative magnetic pole. A secondary bipolar area of silicon enhancement is located closer to the positive magnetic pole between longitudes  $l = 140^\circ$  and  $240^\circ$ . These two spots possibly belong to a ring-like structure encircling the positive magnetic pole.

The chromium distribution was reconstructed simultaneously with the magnetic field map using four unblended Cr II lines and a blend of two Cr II spectral features. Table 4 gives the atomic data for these transitions. For the Cr II lines from the 30th multiplet ( $\lambda$  4812.34, 4824.13 and 4836.23 Å) accurate astrophysical oscillator strengths were derived by Sigut & Landstreet (1990) and are available via VALD. The oscillator strengths of the other Cr II lines were verified by the comparison between spectrum synthesis calculations and observations of the mildly peculiar non-magnetic A stars *o* Peg and 41 Peg. We found it necessary to increase  $\log(gf)$  of the Cr II 5279.88 Å line from  $-2.100$  given in VALD to  $-1.536$ . In the Doppler Imaging based on the Cr II lines belonging to the 30th multiplet and other transitions of ionized chromium we used, respectively, 24 and 27 rotational phases.

Figure 8 shows chromium abundance map and magnetic field distribution recovered from the variations of Stokes *I* and *V* profiles of the six Cr II lines. These maps suggest that, similar to the inversion based on the Si II lines, the rotational modulation of the Cr II spectral lines is consistent with a magnetic topology dominated by a dipole contribution. This is confirmed by the second order multipolar expansion of the final magnetic map, from which we obtained  $B_d = 6.36$  kG,  $\beta_d = 109.7^\circ$ ,  $\gamma_d = 189.7^\circ$  and  $B_q = 1.28$  kG. The chromium abundance image (see Figs. 8 and 12) is characterized by the two large spots of enhanced abundance ( $\log(N_{\text{Cr}}/N_{\text{tot}}) \approx -3.8$ ), which are located roughly at the intersection of the stellar rotational equator and magnetic equator ( $l = 90^\circ$  and  $280^\circ$ ) and are elongated in the latitude direction. A smaller pair of spots is located near the positive magnetic pole ( $l = 140^\circ$  and  $230^\circ$ ) and are connected by a semicircle of chromium overabundance, suggesting that we actually see a ring of chromium around the positive magnetic pole. In contrast, the area around the negative magnetic pole shows depleted Cr abundance ( $\log(N_{\text{Cr}}/N_{\text{tot}}) \approx -6.5$ ).

The observed and computed Stokes *I* and *V* profiles of the Cr II lines are compared in Fig. 6. In addition, in this figure we show the effect of neglecting the magnetic field in synthesizing the variations of the unpolarized spectral lines and the errors in synthetic circular polarization profiles due to the assumption of a homogeneous Cr distribution ( $\log(N_{\text{Cr}}/N_{\text{tot}}) = -5.49$ , which is the average value derived from our Cr abundance map) instead of the true chromium surface map.

The reconstruction of the iron surface distribution and magnetic field topology was based on the analysis of ten Fe II lines from six wavelength regions (four unblended Fe II lines and two groups of Fe II blends). Stokes *I* and *V* profiles from 27 rotational phases were used in the

**Table 5.** Parameters of the second order multipolar expansion of the magnetic maps. Polar strengths of the multipole components are given in kG, while angles specifying orientation of the multipole axes are measured in degrees.

	Si II	Cr II	Fe II	Average
$B_d$	6.14	6.36	6.05	$6.18 \pm 0.16$
$\beta_d$	107.5	109.7	105.3	$107.5 \pm 2.2$
$\gamma_d$	186.5	189.7	185.1	$187.1 \pm 2.4$
$B_q$	1.18	1.28	0.78	$1.08 \pm 0.26$
$\beta_q^1$	89.8	89.0	91.6	$90.1 \pm 1.3$
$\gamma_q^1$	58.8	55.8	51.9	$55.5 \pm 3.5$
$\beta_q^2$	86.2	97.4	99.8	$94.5 \pm 7.3$
$\gamma_q^2$	325.2	326.0	318.9	$323.4 \pm 3.9$

magnetic inversion. Figure 8 presents the resulting iron distribution and a map of the magnetic field geometry. The iron map is also shown in Fig. 12 in the pseudo-Mercator projection. The comparison between observed and computed Stokes *I* and *V* profiles of the Fe II spectral lines is given in Fig. 7.

The magnetic map derived from the Fe II lines was found to be close to a dipole ( $B_d = 6.05$  kG,  $\beta_d = 105.3^\circ$ ,  $\gamma_d = 185.1^\circ$ ) with a minor quadrupole contribution ( $B_q = 0.78$  kG). The iron distribution on the surface of  $\alpha^2$  CVn resembles that of chromium, but has less contrast. Two iron spots ( $\log(N_{\text{Fe}}/N_{\text{tot}}) \approx -2.0$ ) are located at longitudes  $l = 80^\circ$  and  $300^\circ$  and latitude  $b = 15\text{--}30^\circ$ . A secondary group of iron spots at  $l = 150^\circ$  and  $220^\circ$  have comparable areas, but lower iron abundance ( $\log(N_{\text{Fe}}/N_{\text{tot}}) \approx -2.8$ ). These surface features form a semicircle around the negative magnetic pole with a radius smaller than that of the similar chromium structure.

As it was explained in Sect. 4.1, in addition to fitting high-resolution Stokes *I* and *V* profiles, our magnetic DI code models photopolarimetric Balmer line measurements of the disk-average longitudinal magnetic field. Figure 9 compares the observations by Borra & Landstreet (1977) with the predictions of magnetic models, derived from fitting the Si II, Cr II and Fe II lines. All three magnetic distributions provide equally good fits to the existing photopolarimetric longitudinal field measurements.

Table 5 summarizes the parameters of the second order multipolar fit to the magnetic distributions derived from the Si II, Cr II and Fe II spectral lines. In addition to this table, the upper panels in Fig. 12 show rectangular maps of the algebraic average of the radial, meridional and azimuthal components of the magnetic field vector distributions obtained from the lines of silicon, chromium and iron. The dipole and quadrupole parameters of the magnetic geometry obtained from the lines of different chemical elements agree very well. A comparison of the multipolar expansion of the magnetic distributions suggests that the magnetic DI is capable of estimating the polar strength of the dominant dipole magnetic component with an accuracy better than 5%, while a likely error of the

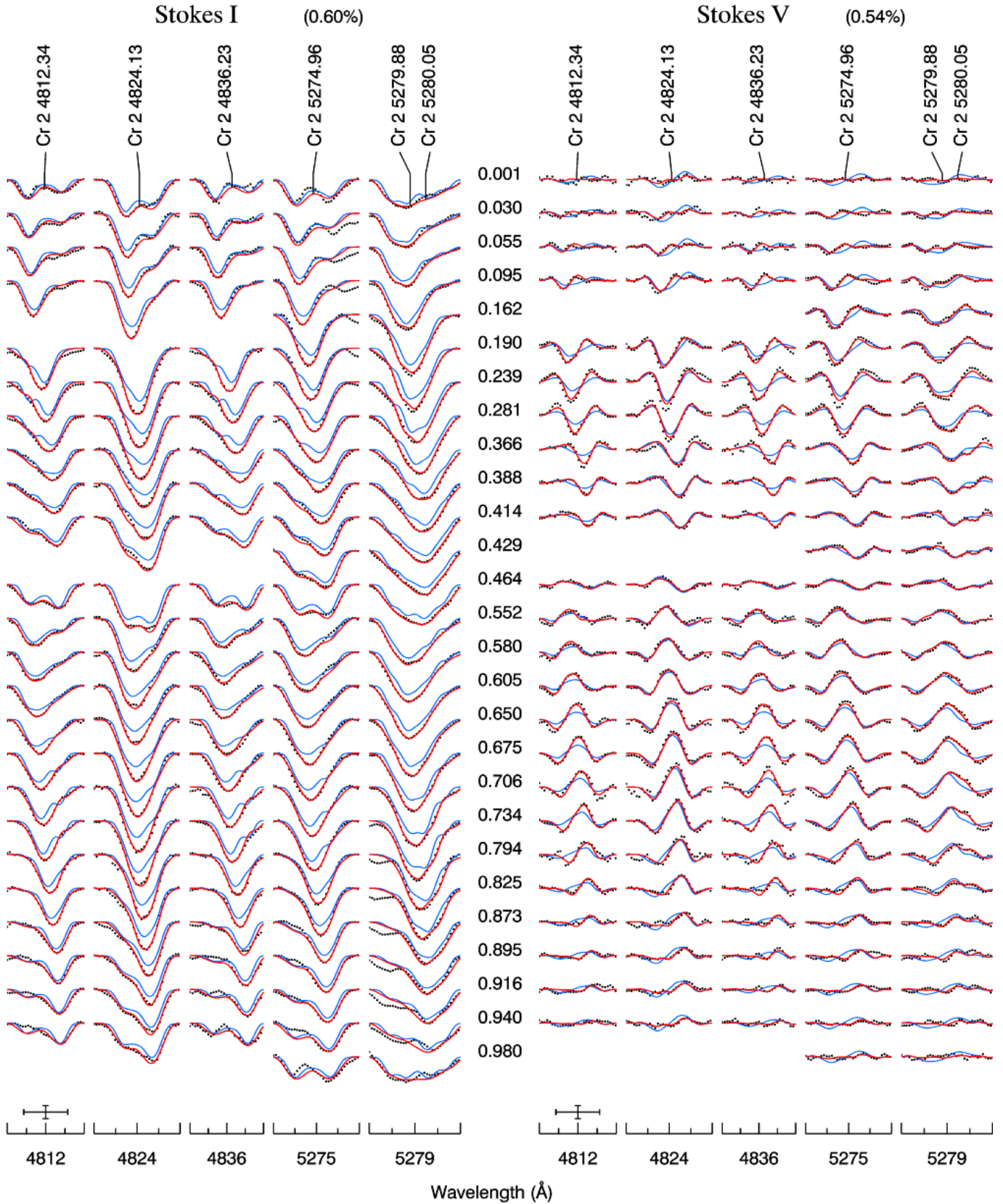


**Fig. 6.** The comparison between observed (dots) and computed (thick lines) Stokes *I* and *V* profiles of the Cr II spectral lines. Spectra for the consecutive rotational phases are shifted in the vertical direction. Rotational phases are indicated in the column to the right of the Stokes *I* panel. The bars at the lower left corner of each panel correspond to 1 Å and 5% of the Stokes *I* continuum intensity. The thin lines in the Stokes *V* panel show circular polarization computed with the optimum magnetic field geometry, but homogeneous Cr abundance distribution. The thin lines in the Stokes *I* panel illustrate the effect of neglecting the magnetic field.

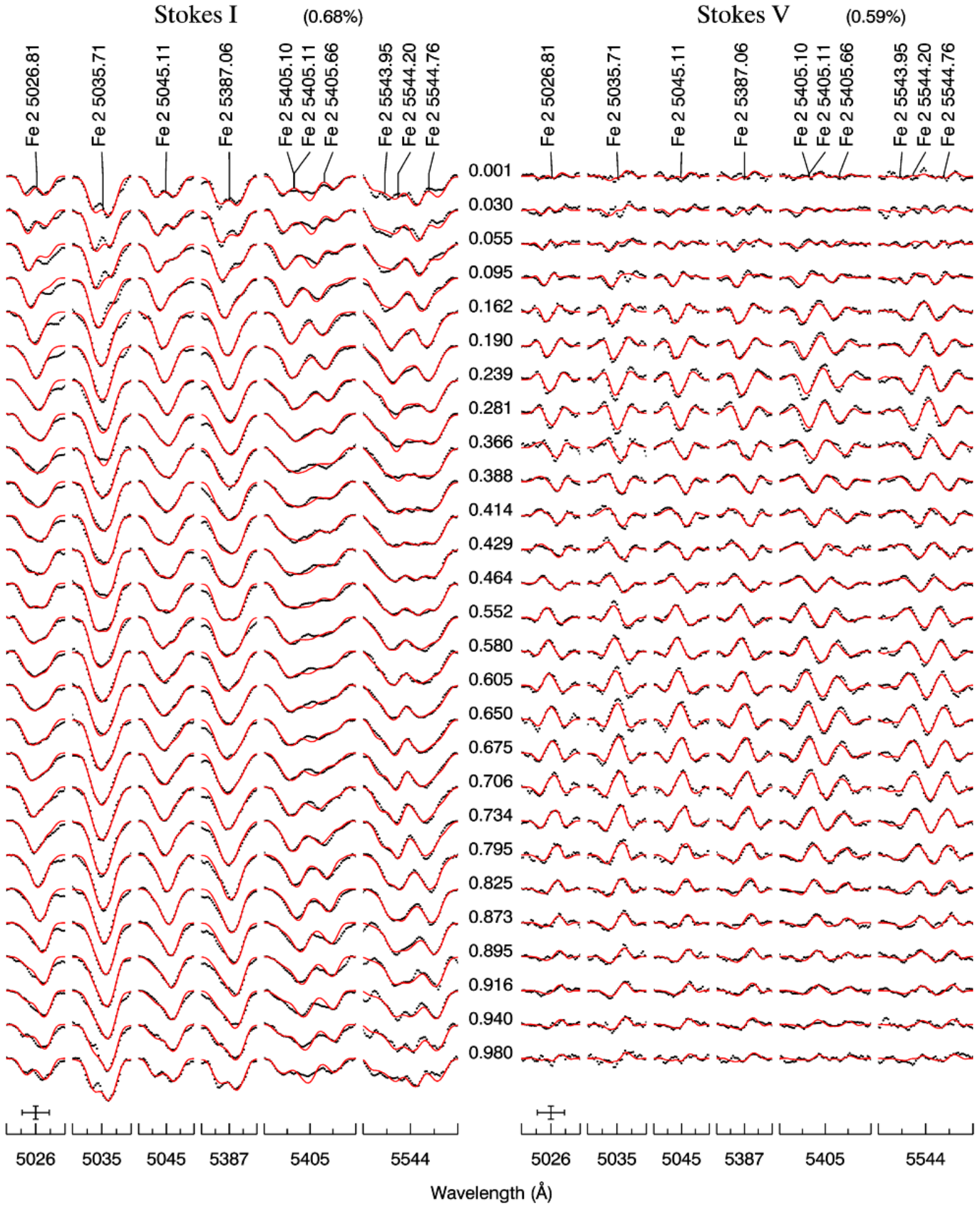
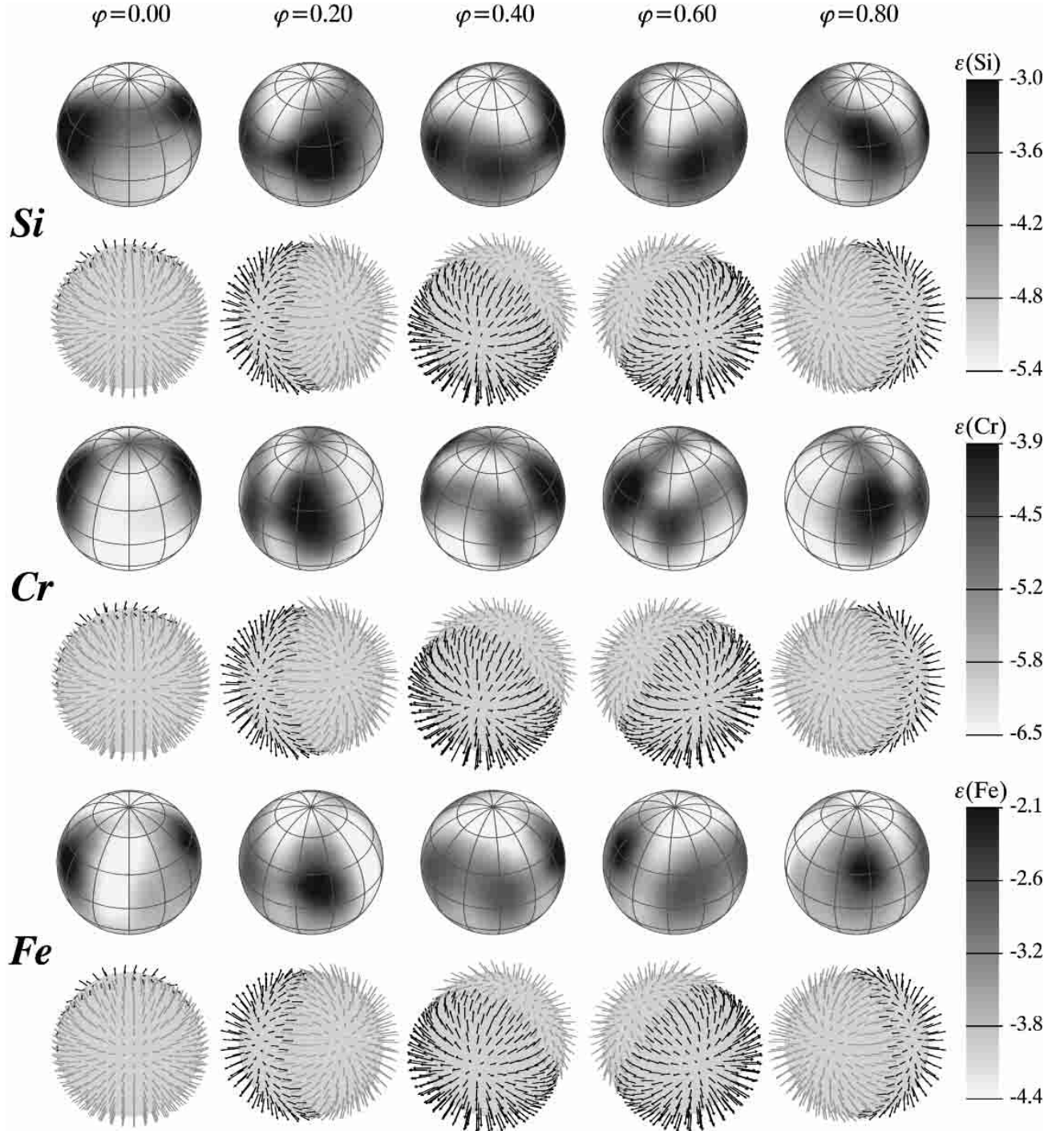


Fig. 7. The same as in Fig. 5, but for the Stokes *I* and *V* profiles of the Fe II spectral lines.



**Fig. 8.** The chemical abundance distributions and magnetic field geometries of  $\alpha^2$  CVn derived from the Stokes  $I$  and  $V$  profiles of the Si lines (two upper rows), Cr lines (two middle rows) and Fe absorption features (two lower rows). The star is shown at 5 equidistant rotational phases, viewed at the inclination angle  $i = 49^\circ 1$ . Each of the three panels visualize an abundance distribution (the upper in each pair of rows) by the greyscale image and the vector magnetic field map (the lower in each pair of rows). On all magnetic maps the black arrows show field vectors pointing outside the stellar surface, while the grey arrows correspond to the vectors pointing inwards. The arrow length is proportional to the field strength.

strength of the smaller quadrupole contribution is limited to 20%. At the same time, the angles specifying the dipole and quadrupole orientations agree to within  $10^\circ$ . Magnetic inversion from the lines of different ions yielded very similar quadrupole strengths and orientations. Therefore,

we believe that this weak deviation from a pure dipole field structure is not an artifact of the inversion process, but reflects real properties of the magnetic field of  $\alpha^2$  CVn.

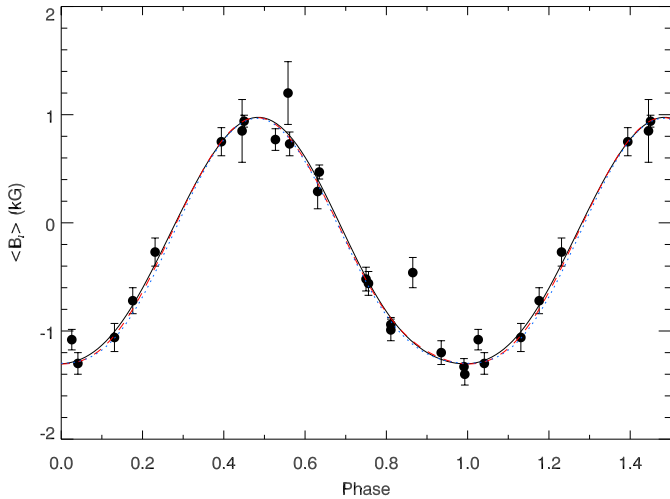


**Fig. 9.** The comparison between photopolarimetric Balmer line measurements (symbols) and longitudinal field variations predicted by the magnetic distributions derived from the Si II (dashed curve), Cr II (dotted curve) and Fe II (solid curve) spectral lines.

#### 4.4. Surface distributions of Cl, Ti and Nd

The very rich spectrum of  $\alpha^2$  CVn gives the possibility to produce detailed maps of the surface abundance distribution of many more chemical species than we studied in the previous Section. In a number of earlier investigations (e.g. Burbidge & Burbidge 1955; Cohen 1970) much attention has been given to the qualitative description of the variations of the  $\alpha^2$  CVn spectral lines, but detailed analysis was not feasible because the presence of the strong magnetic field could not be properly taken into account. With the magnetic field geometry determined in Sect. 4.3 from the iron, silicon and chromium lines, we can now extend DI of  $\alpha^2$  CVn to other chemical elements. In this analysis we used a fixed magnetic topology (the average of the three magnetic maps derived in Sect. 4.3) and reconstructed the surface distributions of chemical abundance using Stokes *I* spectra only. We note, that thorough multi-element abundance DI of  $\alpha^2$  CVn is outside the scope of our paper and can be carried out more efficiently by using high-resolution unpolarized spectra, obtained with one of the numerous échelle spectrographs at medium size telescopes. In this study we limit ourselves to the analysis of the surface maps of a few particularly interesting ions: Cl II, Ti II and Nd III.

Cohen (1970) noted that the lines of singly ionized chlorine behave very similar to the rare-earth spectral features: Cl II lines reach their maximum intensity around phase 0.0 and are very weak at other rotational phases. We confirmed this unexpected behaviour of the chlorine lines and mapped the Cl distribution on the surface of  $\alpha^2$  CVn using the blend of the two Cl II lines:  $\lambda$  4819.48 and 4819.76 Å. A nearby Cl II 4810.07 Å line shows a similar variability pattern, but it is blended by an unidentified line of a rare-earth element (REE) and could not be used in abundance mapping. The VALD database does not contain the Landé factors of the Cl II features that we

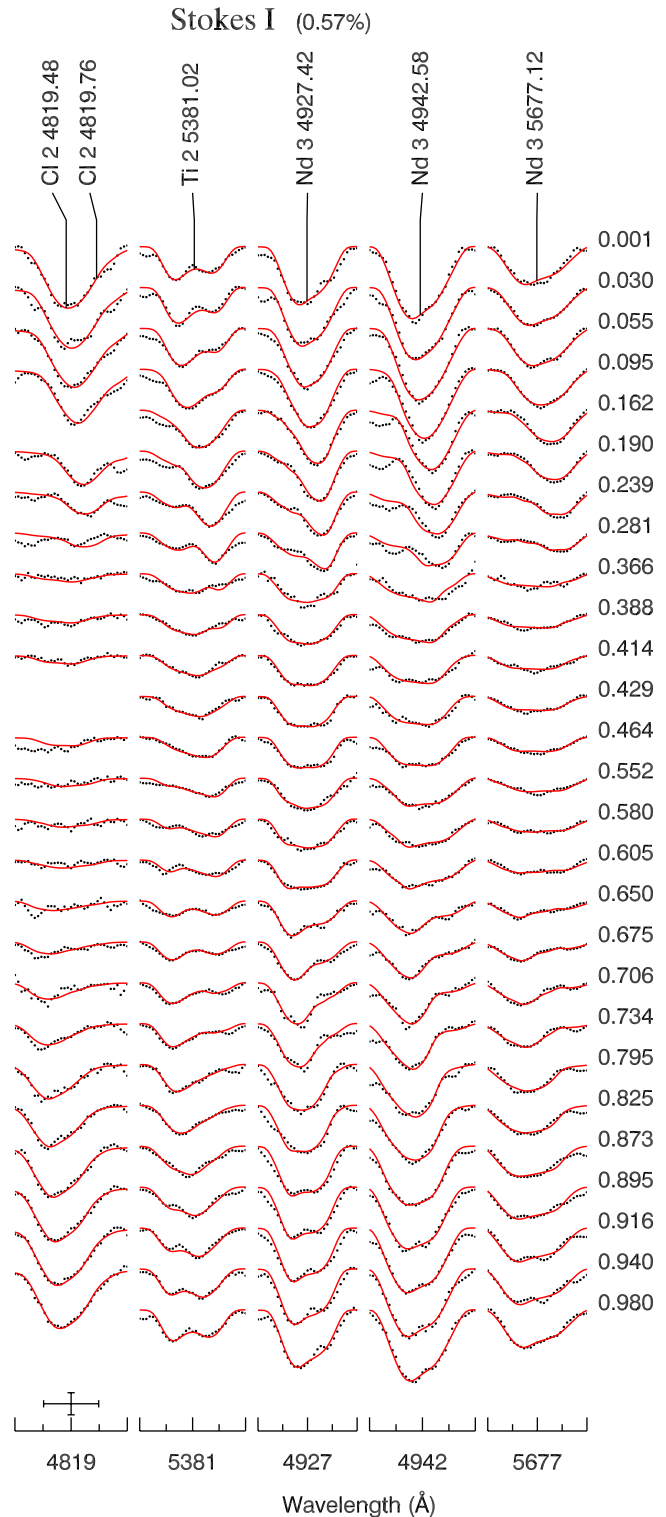


**Fig. 10.** The comparison between observed (dots) and computed (lines) Stokes *I* profiles of the Cl II, Ti II and Nd III spectral lines. Spectra for the consecutive rotational phases are shifted in the vertical direction. Rotational phases are indicated in the column to the right of the Stokes *I* profiles. The bar at the lower left corner corresponds to 1 Å and 5% of the Stokes *I* continuum intensity.

modelled, therefore we computed these essential parameters assuming LS-coupling.

We compare the observed and computed profiles of the Cl II blend in Fig. 10, while the Cl surface map is presented in Figs. 11 and 12. The chlorine distribution is dominated by a large overabundance spot near the negative magnetic pole ( $l = 10^\circ$ ,  $b = 30^\circ$ ), where the local abundance reaches  $\log(N_{\text{Cl}}/N_{\text{tot}}) \approx -1.8$ . In addition, a second area of the weaker chlorine concentration is visible at the opposite rotational phase ( $l = 190^\circ$ ).

Reconstruction of the titanium surface map was based on a single line, Ti II 5381.02 Å. Figure 10 compares our observations of this line with the final fit achieved by INVERS10. The Ti surface map is shown in the spherical projection in Fig. 11 and in the cylindrical equidistant projection in Fig. 12. The titanium distribution is clearly different from the abundance maps of other iron-peak elements (Fe and Cr). It is characterized by a large spot located at the stellar equator and longitude  $l = 310^\circ$ , a second area of Ti overabundance at  $l = 30^\circ$  and  $b = 20^\circ$ , and a low contrast elongated Ti feature above the positive magnetic pole.

$\alpha^2$  CVn is famous for its dramatic changes of the REE line intensity. Earlier Fourier analysis studies (Pyper 1969; Falk & Wehlau 1974) and DI abundance mapping by Goncharskij et al. (1983) focused mostly on Eu II together with other singly ionized REE lines and established a simple picture of the REE surface distribution, according to which a single dominant spot of REE overabundance is located at or near the negative magnetic pole of  $\alpha^2$  CVn. It has become a general consensus that all rare-earth elements (plus chlorine) in the atmosphere of  $\alpha^2$  CVn follow this pattern. In our spectroscopic material we also see numerous weak REE features appearing at phase 0.0, but the limited wavelength coverage of our SOFIN observations does not allow to identify any strong singly ionized REE lines suitable for the abundance DI. However, we were able to identify a number of doubly ionized Nd absorption features, of which Nd III 4927.5 and 5677.1 Å appeared particularly useful for mapping. Furthermore, we noticed an unblended line at  $\lambda$  4942.6 Å, that looked very similar to the Nd III 4927.5 Å. The fact, that this feature is strong in Nd-rich cool Ap star 33 Lib and was identified as neodymium by Crosswhite (1976), suggests that this line indeed belongs to Nd III. One possibility would be a transition with  $\log(gf) = -1.18$  from the 5093.3 cm<sup>-1</sup> level to the predicted level at 25062.3 cm<sup>-1</sup> (Bord 2000). Parameters of the upper level are poorly known, which explains the large discrepancy between the predicted wavelength and the observed one. We tried to improve the relative agreement of the wavelengths of the three Nd III lines by fitting the average  $\alpha^2$  CVn spectrum. The resulting wavelengths are listed in Table 4. At the same time, we did not find it necessary to alter the oscillator strengths of these Nd III lines with respect to the  $\log(gf)$ s computed by Bord (2000) and distributed via VALD.

The comparison between the observed and computed profiles of the Nd III lines is shown in Fig. 10 for 27 rotational phases. The neodymium surface map, presented in Figs. 11 and 12, confirms our suspicion that the Nd III

distribution differs substantially from a single spot surface pattern, typical for singly ionized REE. The Nd III image is dominated by a spot of overabundance at  $l = 340^\circ$  and  $b = 15^\circ$  and a second smaller feature at the rotational equator and  $l = 50^\circ$ . These two neodymium spots, in which we find the Nd abundance  $\log(N_{\text{Nd}}/N_{\text{tot}}) \approx -6.4$ , are responsible for the asymmetric two-component structure of the Nd III line profiles at the phase of REE maximum. In addition, a third area with not so prominent Nd overabundance is located close to the positive magnetic pole ( $l = 150\text{--}230^\circ$ ).

## 5. Discussion

### 5.1. Horizontal diffusion models

The magnetic DI of  $\alpha^2$  CVn presented in this paper is aimed at better understanding of the interplay between the magnetic and abundance surface structures and hence the mechanism of the horizontal and vertical chemical diffusion in the magnetized stellar atmosphere. The magnetic and abundance surface maps, such as those presented in Fig. 12, should be compared with detailed time-dependent theoretical diffusion calculations in order to identify processes governing the evolution of the surface abundance distributions. Unfortunately, even the most recent theoretical diffusion calculations are only able to grasp some general trends in chemical peculiarities of the magnetic stars, but are not detailed enough to be useful for explaining high-resolution DI surface abundance maps. We hope that our investigation of  $\alpha^2$  CVn and subsequent simultaneous magnetic and abundance imaging of other strongly magnetic CP stars will stimulate new more detailed and more sophisticated theoretical diffusion studies, and here we only limit ourselves to the qualitative comparison of our results with a few available predictions of the horizontal diffusion models.

Firstly, we note that all abundance maps that we derived for  $\alpha^2$  CVn show some degree of correlation with the magnetic topology. The most clear examples are chlorine, which is mostly concentrated near the negative magnetic pole, and chromium forming a ring around the positive magnetic pole. However the surface abundance distributions cannot be reduced to a combination of rings and polar caps symmetric with respect to the magnetic field geometry. For example, the Ti as well as Nd maps are dominated by the two unequal spots located on both sides of the negative magnetic pole, and *all* abundance distributions are characterized by the major overabundance areas located roughly between latitudes  $b = 0^\circ$  and  $b = 45^\circ$ . This hints that, in order to produce the observed surface structures, the horizontal diffusion due to the magnetic field must be affected by some other phenomena. One possibility would be an interaction between the magnetic field, mass loss and rotation. A weak stellar wind of the order of  $10^{-13}\text{--}10^{-15} M_\odot \text{ yr}^{-1}$  and constrained by the magnetic field was proposed by Babel & Michaud (1991) and Babel (1992) in order to explain the abundance maps

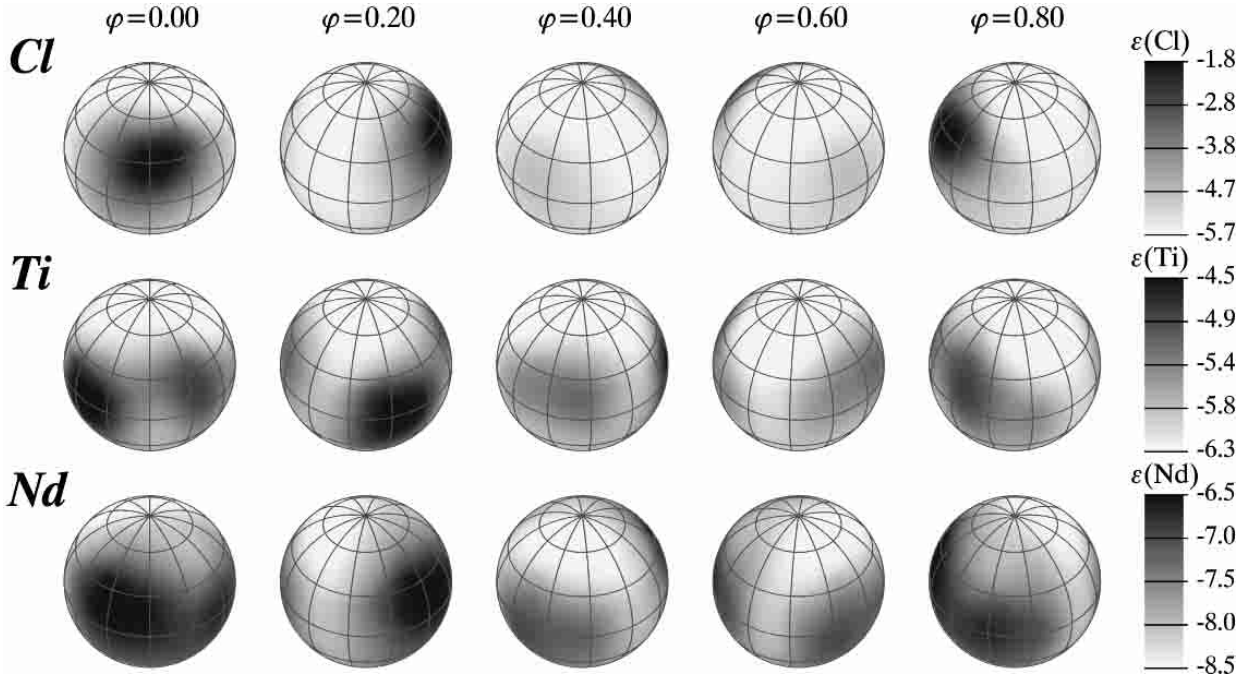


**Fig. 11.** The same as in Fig. 8, but for the chemical abundance distributions of Cl (the upper row), Ti (the middle row) and Nd (the lower row).

derived for 53 Cam by Landstreet (1988). On the other hand, from the studies of the mass loss from other types of stars we know that even low rotation rates could significantly modify the structure of the mass outflow (e.g. Dorfi & Höfner 1996). Therefore, it seems not completely inconceivable that the stellar wind confined by the magnetic field and altered by the stellar rotation could play a role in creating the abundance patterns on the surface of  $\alpha^2$  CVn.

Vauclair et al. (1991) examined He diffusion for main sequence magnetic stars with a dipolar magnetic field. Their model predicts a strong helium underabundance at the magnetic equator, which is consistent with the factor of  $10^3$  He depletion discovered for  $\alpha^2$  CVn in our study. Vauclair et al. (1991) showed that a strong enough stellar wind can prevent He depletion at the magnetic poles. Thus, within the framework of this He diffusion model, the absence of the He absorption at  $\lambda$  5876 Å discussed in Sect. 3 sets an upper limit of  $\sim 2 \times 10^{-13} M_{\odot} \text{ yr}^{-1}$  on the rate of the possible mass loss of  $\alpha^2$  CVn.

The horizontal and vertical diffusion of silicon in the presence of a global magnetic field received much attention in the studies by Alecian & Vauclair (1981), Michaud et al. (1981) and Mégessier (1984). In the latter investigation, the time-dependent surface distribution of Si was modelled, and silicon was found to be overabundant over most of the stellar surface and to migrate from the magnetic equator towards the magnetic poles on time scales comparable with the lifetime on the main sequence. This picture agrees well with the Si map obtained in our study.  $\alpha^2$  CVn has roughly a factor of 2 average Si overabundance relative to the solar chemical composition, and for the intermediate age of  $\alpha^2$  CVn we see that the initial

Si enhancement along the magnetic equator has largely disappeared and the element is concentrated in ring-like structures encircling the magnetic poles. We expect that after some  $(5-9) \times 10^8$  years Si will form two overabundance areas close to the positions of the present magnetic poles.

No general theoretical calculations of the horizontal diffusion are available for the other chemical elements studied in our paper (Cl, Ti, Cr, Fe and Nd).

## 5.2. Magnetic DI versus other methods of reconstructing stellar magnetic fields

Currently the structure of the magnetic field on the surfaces of CP stars is most often inferred from an analysis of the so-called *magnetic field observables*. These surface averaged magnetic field estimates typically include the mean longitudinal magnetic field (Mathys 1991), the mean magnetic field modulus (Mathys et al. 1997), the mean quadratic magnetic field (Mathys 1995a) and the crossover (Mathys 1995b). These parameters are usually derived from the medium resolution, low  $S/N$  measurements of the circular polarization and intensity of the metallic absorption lines. For a few stars the net linear polarization observations through a broadband filter are also available (Leroy 1995). A joint analysis of the magnetic observables (e.g. Bagnulo et al. 1999; Landstreet & Mathys 2000) usually assumes some form of a global multipolar field parameterization and does not take into account any inhomogeneous surface distribution of chemical elements. Our study of the high-resolution, high  $S/N$  Stokes  $I$  and  $V$  profiles of  $\alpha^2$  CVn suggests that neglecting abundance spots in the interpretation of the magnetic

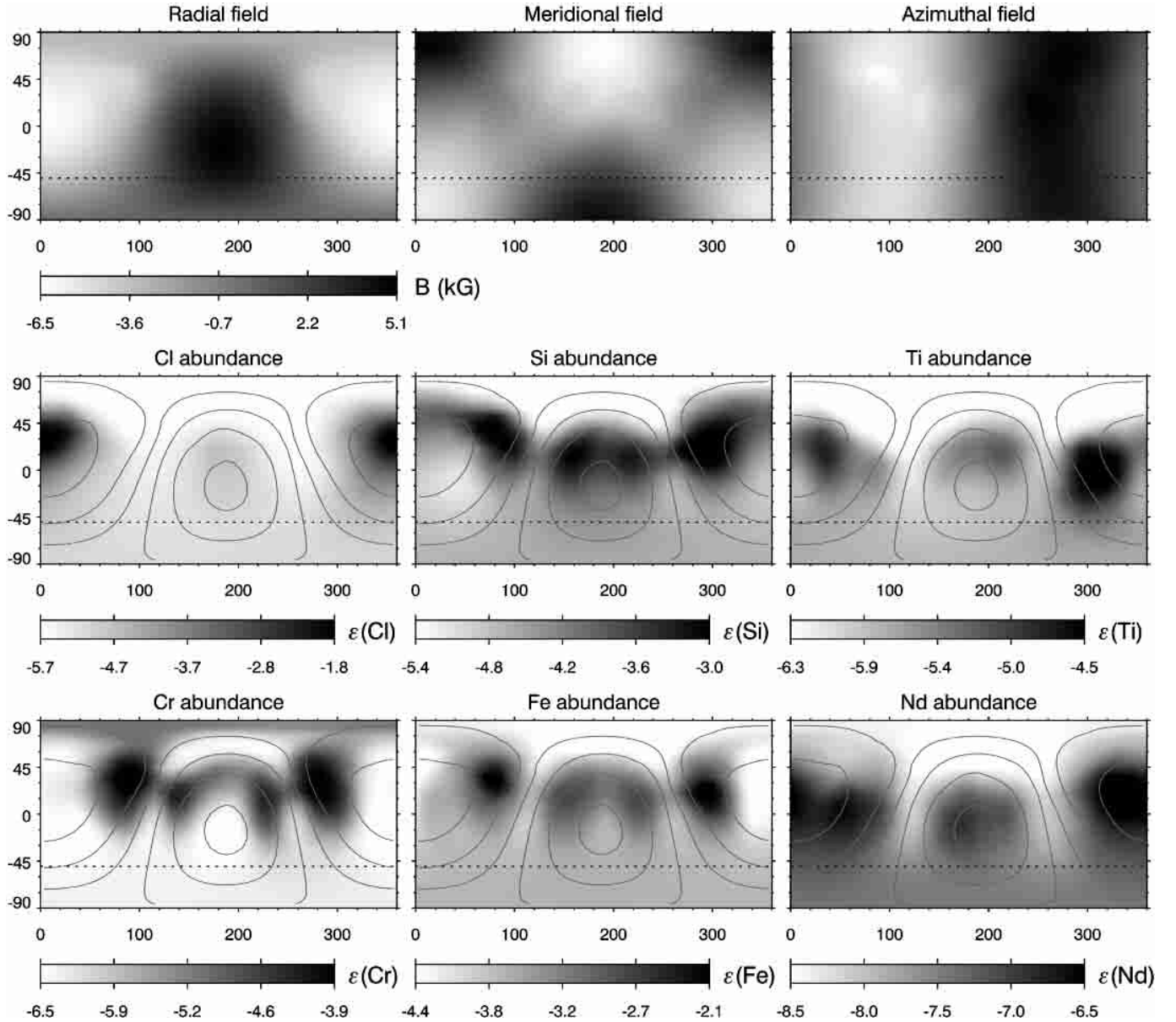


**Fig. 12.** The cylindrical equidistant projection of the surface maps of the radial, meridional and azimuthal components of the vector magnetic distribution obtained by averaging the magnetic images, derived from the Si II, Cr II and Fe II lines (the upper three panels). This average magnetic map is compared with the surface abundance distributions of singly ionized Cl, Si, Ti, Cr, Fe and doubly ionized Nd (the lower six panels). The solid curves shown on top of the abundance maps are the contours of equal radial field, plotted for the field values between  $-6$  and  $4$  kG with a  $2$  kG step. The horizontal dotted line in each panel indicates the lowest visible latitude for the inclination angle  $i = 49^\circ$  adopted in our study.

measurements can severely affect field mapping. Figure 6 shows for the example of the Cr II lines that abundance non-uniformities have a strong effect on both the amplitude and the shape of the Stokes  $V$  profiles. Similar conclusions have been reached by Wade et al. (2000b), who found a large discrepancy between the longitudinal field of  $\alpha^2$  CVn derived from the iron and chromium lines and the Balmer line photopolarimetric measurements. The presence of abundance spots introduces an additional modulation in the phase curves of the magnetic observables obtained from the metallic lines. As a result, non-sinusoidal variations of, for example, the mean longitudinal field

appear and are often erroneously interpreted as an evidence for a strong quadrupolar contribution to the topology of the stellar magnetic fields. In this way a simple-minded fit of the magnetic model consisting of an aligned dipole and a linear quadrupole to the very accurate metallic line longitudinal field measurements reported for  $\alpha^2$  CVn by Wade et al. (2000b) yields  $B_q/B_d \approx 2.5$ : more than a factor of 10 increase in the ratio of quadrupole to dipole strength ratio in comparison with the results of our magnetic DI modelling (see Table 5)! Not surprisingly, magnetic models built on the basis of an interpretation of the magnetic observables affected by the chemical surface

inhomogeneities fail when confronted with the high  $S/N$  observations in Stokes parameters (Bagnulo et al. 2001).

We suggest that much more caution should be exercised when interpreting magnetic observables inferred from the metallic lines. Complex and incoherent variations of the magnetic observables with rotational phase may be indicative of abundance spots rather than hint on unusual magnetic geometry, especially when Balmer line photopolarimetry shows nearly sinusoidal variations of the longitudinal field and the star in question is a known spectrum variable. Clearly, the only way to verify the reliability of the magnetic models for such stars is to compare model predictions with high-resolution spectra in several Stokes parameters. Furthermore, our study of  $\alpha^2$  CVn demonstrated that advances in the observational and modelling techniques make it possible to extract the full information about the abundance and magnetic surface structures directly from such spectropolarimetric observations.

In conclusion we note, that magnetic Doppler Imaging of  $\alpha^2$  CVn presented in this paper was based exclusively on high quality Stokes  $I$  and  $V$  observations. Further improvements of the quality of the magnetic imaging can be achieved by modelling high  $S/N$  and high-resolution linear polarization observations. We expect that using complete Stokes vector datasets would make it possible to ease restrictions imposed by the multipolar regularization and possibly resolve finer details of the stellar surface magnetic distribution. It will also allow us to improve magnetic reconstruction in the surface areas where magnetic field appears nearly tangential relative to the line-of-sight during most of the rotational period. However, based on numerical experiments of magnetic DI (Paper II), we consider it quite unlikely that for relatively simple magnetic geometry of  $\alpha^2$  CVn incorporating Stokes  $Q$  and  $U$  spectra in magnetic inversion would result in any significant changes of the global magnetic properties (i.e. parameters of the dipolar magnetic component) or would noticeably modify surface abundance maps.

*Acknowledgements.* This work was supported by the Swedish National Research Council. We would like to thank the Knut and Alice Wallenberg Foundation for contributing to the state-of-the-art computing facilities at the Institute of Astronomy and Space Physics in Uppsala. We are also grateful to Eric Stempels and Paul Barklem for their assistance in obtaining and reducing MUSICOS data. We greatly appreciate the help by Rudolf Duemmler, whose numerous comments and corrections were very useful in improving the text of our paper.

This research has made extensive use of the SIMBAD database, operated at CDS, Strasbourg, France.

## References

- Adelman, S. J., Pyper, D. M., Shore, S. N., White, R. E., & Warren, W. H. 1989, *A&AS*, 81, 221
- Alecian, G., & Vauclair, S. 1981, *A&A*, 101, 16
- Auer, L. H., Mihalas, D., Aller, L. H., & Ross, J. E. 1966, *ApJ*, 145, 153
- Babel, J., & Michaud, G. 1991, *ApJ*, 366, 560
- Babel, J. 1992, *A&A*, 258, 449
- Babu, G. S. D., & Shylaja, B. S. 1981, *Ap&SS*, 79, 243
- Bagnulo, S., Landolfi, M., & Landi Degl’Innocenti, M. 1999, *A&A*, 343, 865
- Bagnulo, S., & Landolfi, M. 1999, *A&A*, 346, 158
- Bagnulo, S., Wade, G. A., Donati, J.-F., et al. 2001, *A&A*, 369, 889
- Barklem, P. S., Stempels, H. C., Allende Prieto, C., et al. 2002, *A&A*, 385, 951
- Bord, D. J. 2000, *A&AS*, 144, 517
- Borra, E. F., & Landstreet, J. D. 1977, *ApJ*, 212, 141
- Burbidge, G. R., & Burbidge, E. 1955, *ApJS*, 1, 431
- Cohen, J. G. 1970, *ApJ*, 159, 473
- Crosswhite, H. 1976, private communication
- Deutsch, A. 1958, in *Electromagnetic Phenomena in Cosmical Physics*, ed. B. Lehnert, IAU Symp. No. 6, 209
- Dorfi, E. A., & Höfner, S. 1996, *A&A*, 313, 605
- ESA 1997, *The Hipparchos Catalogue*, ESA SP-1200
- Falk, A. E., & Wehlau, W. H. 1974, *ApJ*, 192, 409
- Farnsworth, G. 1932, *ApJ*, 75, 364
- Flower, P. J. 1996, *ApJ*, 469, 355
- Glagolevskij, Yu. V., Piskunov, N. E., & Khokhlova, V. L. 1985, *PAZh*, 11, 371
- Gómez, A. E., Luri, X., Grenier, S., et al. 1998, *A&A*, 336, 953
- Gonchariskij, A. V., Ryabchikova, T. A., Stepanov, V. V., Khokhlova, V. L., & Yagola, A. G. 1983, *AZh*, 60, 83
- Ilyin, I. V., & Duemmler, R. 1999, in *Precise Stellar Radial Velocities*, ed. J. B. Hearnshaw, & C. D. Scarfe, ASP Conf. Ser., 185, 63
- Ilyin, I. V. 2000, Ph.D. Thesis, Oulu University
- Khokhlova, V. L., & Pavlova, V. M. 1984, *PAZh*, 10, 377
- Kochukhov, O., & Piskunov, N. 2002, *A&A*, 388, 868, Paper II
- Kupka, F., Piskunov, N., Ryabchikova, T. A., Stempels, H. C., & Weiss, W. W. 1999, *A&AS*, 138, 119
- Kurucz, R. 1993, CD-ROM, No. 13, *Smithsonian Astrophys. Obs.*
- Kuschnig, R., Ryabchikova, T. A., Piskunov, N. E., Weiss, W. W., & Gelbmann, M. J. 1999, *A&A*, 348, 924
- Landolfi, M., Bagnulo, S., & Landi Degl’Innocenti, M. 1998, *A&A*, 338, 111
- Landstreet, J. D., Borra, E. F., Angel, J. R. P., & Illing, R. M. E. 1975, *ApJ*, 201, 624
- Landstreet, J. D. 1988, *ApJ*, 326, 967
- Landstreet, J. D. 1992, *A&AR*, 4, 35
- Landstreet, J. D., & Mathys, G. 2000, *A&A*, 359, 213
- Leone, F., & Manfrè, M. 1997, *A&A*, 320, 257
- Leroy, J. L. 1995, *A&AS*, 114, 79
- Mathys, G. 1991, *A&AS*, 89, 121
- Mathys, G. 1995a, *A&A*, 293, 746
- Mathys, G. 1995b, *A&A*, 293, 733
- Mathys, G., Hubrig, S., Landstreet, J. D., Lanz, T., & Manfroid, J. 1997, *A&AS*, 123, 353
- Mégevrier, C. 1984, *A&A*, 138, 267
- Michaud, G. 1970, *ApJ*, 160, 641
- Michaud, G., Mégevrier, C., & Charland, Y. 1981, *A&A*, 103, 244
- Peterson, D. M. 1969, *Smithsonian Astrophys. Obs. Spec. Rep.*, 293
- Plachinda, S. I., & Tarasova, T. N. 1999, *ApJ*, 514, 402
- Piskunov, N. E. 1992, in *Stellar Magnetism*, ed. Yu. V. Glagolevskij, & I. I. Romanyuk, Nauka, St. Petersburg, 92
- Piskunov, N., & Kupka, F. 2001, *ApJ*, 547, 1040
- Piskunov, N., & Kochukhov, O. 2002, *A&A*, 381, 736
- Pyper, D. M. 1969, *ApJS*, 18, 347

- Ryabchikova, T., Piskunov, N., Savanov, I., Kupka, F., & Malanushenko, V. 1999, *A&A*, 343, 229
- Schaller, G., Schaerer, D., Meynet, G., & Maeder, A. 1992, *A&AS*, 96, 269
- Shallis, M. J., Baruch, J. E. F., Booth, A. J., & Selby, M. J. 1985, *MNRAS*, 213, 307
- Sigut, T. A., & Landstreet, J. D. 1990, *MNRAS*, 247, 611
- Sobelman, I. I. 1979, *Atomic Spectra and Radiative Transitions*, Springer Series in Chemical Physics, vol. 1 (Springer-Verlag, Berlin)
- Stehlé, C. 1994, *A&AS*, 104, 509
- Stępień, K. 1978, *A&A*, 70, 509
- Stibbs, D. W. N. 1950, *MNRAS*, 110, 395
- Takeda, Y., Takada-Hidai, M., Jugaku, J., Sakaue, S., & Sadakane, K. 1999, *PASJ*, 51, 961
- Tuominen, I., Ilyin, I., & Petrov, P. 1999, in *Astrophysics with the NOT*, ed. H. Karttunen, & V. Piirola, University of Turku, Tuorla Observatory, 47
- Vauclair, S., Dolez, N., & Gough, D. O. 1991, *A&A*, 252, 618
- Vidal, C. R., Cooper, J., & Smith, E. W. 1973, *ApJS*, 25, 37
- Wade, G. A., Donati, J.-F., Landstreet, J. D., & Shorlin, S. L. S. 2000a, *MNRAS*, 313, 823
- Wade, G. A., Donati, J.-F., Landstreet, J. D., & Shorlin, S. L. S. 2000b, *MNRAS*, 313, 851
- Wallace, L., Hinkle, K., & Livingston, W. 2000, *An Atlas of the Spectrum of the Solar Photosphere*, NOAO
- Žižňovský, J., & Zverko, J. 1995, *Contrib. Astron. Obs. Skalnaté Pleso*, 25, 39